Supporting Information

Homogenous metallic deposition regulated by defect-rich skeletons for sodium metal batteries

Zhen Xu,[a†] Zhenyu Guo,[a†] Rajesh Madhu,[a] Fei Xie,[b] Ruixuan Chen,[a] Jing Wang,[c] Mike Tebyetekerwa,[d] Yong-Sheng Hu[b] and Maria-Magdalena Titirici[a]*

[a] Department of Chemical Engineering, Imperial College London, South Kensington Campus, London SW7 2AZ, United Kingdom

[b] Beijing Key Laboratory for New Energy Materials and Devices, Beijing National Laboratory for Condensed Matter Physics, Institute of Physics, Chinese Academy of Sciences, Beijing 100190, China

[c] Bristol Composites Institute (ACCIS), School of Civil, Aerospace, and Mechanical Engineering, University of Bristol, Bristol BS8 1TR, UK

[d] School of Engineering, College of Engineering and Computer Science, The Australian National University, Canberra, ACT 2601, Australia

[†] These authors contributed equally towards this work

* Corresponding author: Prof. Maria-Magdalena Titirici. Email: m.titirici@imperial.ac.uk

Experimental section

1. Materials

1.1. Preparation of lignin nanofibre mats

The preparation of the carbon nanofibre skeletons was based on a reported study from our group.[1-3] First, 80 mg of sodium hydroxide (NaOH, pellets, Fisher Scientific) was dissolved in 4 mL of deionised (DI) water to prepare 0.5 M aqueous NaOH solution. Then, 66.3 mg of polyethylene oxide (PEO, Mw ~600000 g mol^{-1}, Sigma-Aldrich) was added to the mixed solution of 4 mL of home-made 0.5 M NaOH solution and 1 mL of acetone (Sigma-Aldrich), followed by adding 596.7 mg of organosolv lignin (OSL) into the solution. The whole preparation process of the electrospinning solution was kept under continuous magnetic stirring until all the components were well dispersed. The spinning solution was centrifuged for 5 min at 5000 rpm to remove air bubbles before transferring to a syringe with an 18 Gauge needle. Subsequently, the homogenous solution was electrospun at a rate of 1.2 mL h^{-1} under an electric field of 20 kV with a distance of 25 cm from the needle to an aluminium (Al) collector. The whole electrospinning process was performed in a chamber (Nanobox, Plaslab) with a controlled temperature of 25 ^{o}C and a controlled humidity of 20%. After spinning 5 mL of solution, the lignin mats (around 100 µm thickness) were collected from the collector and cut into stripes for further utilisation.

1.2 Preparation of carbon nanofibre skeletons

The lignin mats were sandwiched between two ceramic plates, followed by transferring lignin mats to a Carbolite tubular furnace. The lignin mats were then heated to different temperatures (700 ^{o}C, 1100 ^{o}C and 1500 ^{o}C) for 2 h with a ramp rate of 5 ^{o}C min^{-1} under an N_2 atmosphere. The carbonised carbon nanofibre skeletons (about 50 µm thickness) were washed in 80 ^{o}C DI water for 2 h to remove residual impurities and then dried in an oven at 80 ^{o}C for 1 h. Finally, the carbon skeletons were cut into small pieces (8 mm in diameter) and further dried at 80 ^{o}C overnight under vacuum. These carbonised lignin mats at different temperatures were noted as L700, L1100 and L1500, respectively.

1.3 Preparation of Na/C composite anodes

To test the symmetric cells and full cells, the Na/C composite anodes were prepared by pre-deposition of a small amount of metallic sodium onto the carbon skeletons at room temperature. The electrodeposition method can precisely control the amount of metallic sodium on the carbon skeletons by regulating the current density and deposition time, which is beneficial to scientific research and comparison. The deposited metallic sodium is more glassy with enhanced electron and ionic conductivity.[4] A piece of carbon skeleton (8 mm in diameter) and a piece of metallic sodium (8 mm in diameter) were separated by a glass fibre membrane (16 mm in diameter, GF/D Glass microfibre filters, Whatman) soaked in 200 µL of 1 M $NaCF_3O_3$ in diglyme. Stainless steel coin cells (CR2032, MTI Corporation) were pressed using a crimping machine (MTI Corporation). The

pre-deposition in the half cell configuration was conducted at a current density of 1.0 mA g^{-1} for 8 h using a LAND CT 3001A battery testing system, followed by the disassembly of the coin cell. The pre-deposited Na/C composite anodes were cleaned by washing with diglyme solvent and dried for further electrochemical testings. The assembly and disassembly of coin cells were both performed in an Argon-filled glove box (H_2O, O_2 < 0.5 ppm, mBraun).

1.4 Preparation of Prussian blue cathode

Prussian blue was prepared based on the method reported by Guo *et al.*[5] 0.968 g of sodium ferrocyanide decahydrate ($Na_4Fe(CN)_6 \cdot 10\ H_2O$, Sigma-Aldrich) and 1 mL of hydrochloric acid (37 % HCl, Sigma-Aldrich) were dissolved in 100 mL of DI water to form a homogenous solution. Then, the solution was under a continuous magnetic stirring at 60 °C for 4 h to form Prussian blue crystals within the solution. Such mixed solution was centrifuged at 10000 rpm for 15 min, after which the supernatant was then removed. The sediments of Prussian blue crystals were washed with DI water. The centrifugation and washing were repeated several times to fully remove the residual impurities. Finally, the yielded sediments of Prussian blue crystals were dried firstly at 120 °C in an ambient oven for 12 h and then at 100 °C in a vacuum oven overnight. The Prussian blue cathode was prepared by coating a mixed slurry of 60 wt% Prussian blue crystals, 30 wt% acetylene black (Sigma-Aldrich), and 10 wt% polyvinylidene difluoride (PVDF, Sigma-Aldrich) in 1-Methyl-2-pyrrolidinone (NMP, Sigma-Aldrich) onto Al foil (MTI Corporation). Then, the coated foil was dried at 50 °C in an ambient oven and then at 120 °C in a vacuum oven overnight, before being cut into pieces of electrodes for further battery assembly. The loading mass of active materials on Al foils was controlled between 2.0 and 2.5 mg cm^{-2}.

1.5 Preparation of sulfur cathode

The sulfur cathode was prepared based on the method reported by Miao *et al.*[6] The bare sulfur cathodes were prepared by coating a mixed slurry of 60 wt% sulfur, 30 wt% acetylene black (Sigma-Aldrich), and 10 wt% polyvinylidene difluoride (PVDF, Sigma-Aldrich) in 1-Methyl-2-pyrrolidinone (NMP, Sigma-Aldrich) onto Al foils (MTI Corporation). Then, the coated foil was dried at 50 °C in an ambient oven and then at 50 °C in a vacuum oven overnight, before being cut into pieces of electrodes for further battery assembly. The loading mass of active materials on Al foils was controlled between 1.0 and 1.5 mg cm^{-2}. For the sulfur/carbon composite cathodes (S/L1500), the mixture of sulfur and L1500 in a mass ratio of 40:20 covered by the Al foil was put into a stainless-steel autoclave which was then heated to 155 °C for 12 h in a hydrothermal oven to allow the infiltration of sulfur into the porous carbon skeleton. After that, the S/L1500 composite cathodes were prepared by coating a mixed slurry of the yielded mixture, acetylene black (Sigma-Aldrich), and polyvinylidene difluoride (PVDF, Sigma-Aldrich) in 1-Methyl-2-pyrrolidinone (NMP, Sigma-Aldrich) with a mass ratio of 60:30:10 onto Al foils (MTI Corporation) as well. Then, the coated foil was also dried slowly at 50 °C in an ambient oven and then at 50 °C in a vacuum oven overnight, before being cut into pieces of electrodes for further battery assembly. The loading mass of active

materials on Al foils was controlled between 1.0 and 1.5 mg cm^{-2} too.

2. Materials Characterisation

First, the scanning electron microscopy (SEM, LEO Gemini 1252 FEG-SEM machine) and transmission electron microscope (TEM, JEOL 2010) were employed to characterise the morphology of samples. For SEM, samples were placed onto stainless steel stubs with a double-sided conductive carbon tape, while for TEM, samples were dispersed in ethanol solution to obtain a diluted dispersion which can be dropped onto holey carbon grids (Agar Scientific). For the ex-situ SEM testing of cycled samples, the samples were first plated and stripped for 10 cycles, followed by a further plating process, at the current density of 1.0 mA cm^{-2} with a specific capacity of 2.0 mAh cm^{-2} using a LAND CT 3001A battery testing system. The cycled samples were then disassembled in an Argon-filled glove box (H_2O, O_2 < 0.5 ppm, mBraun) and loaded onto a sealed tube before being transferred into the testing chamber of SEM to avoid contaminations and oxidation. The element mapping of Na/C composite anodes mentioned above was also conducted using the LEO Gemini 1252 FEG-SEM machine.

The Raman Spectroscopy was utilised to analyse the defect structures of carbon materials using a Renishaw inVia Raman instrument with a laser wavelength of 532 nm, and the fitting of Raman spectra was based on the Lorentzian model. Three different areas of each sample were detected and averaged. The average in-plane distances (L_a) were calculated from the intensity ratio of the D- and G-peaks. The *operando* Raman testing was further conducted using the built-in continuous scanning mode of the same Renishaw inVia Raman instrument with a light wavelength of 532 nm. The configuration of the *operando* Raman cell is shown in Figure S15 which was assembled in an Argon-filled glove box (H_2O, O_2 < 0.5 ppm, mBraun) with 1 M $NaCF_3SO_3$ in diglyme. During the continuous scanning of the samples, the *operando* Raman cell was simultaneously discharged at a current density of 0.5 mA cm^{-2} for 4 h using a LAND CT 3001A battery testing system, and the Raman beam was focused on a fixed spot on the surface of carbon materials during testing.

The N_2 adsorption/desorption isotherm of carbon materials was measured at 77 K to analyse the pore structures of carbon materials using a Micromeritics 3 Flex Physisorption instrument, followed by the evaluation of the surface area and pore size distribution based on the multipoint Brunauer-Emmett-Teller (BET) method and non-local density-functional-theory (NLDFT) method from the adsorption part of the isotherm, respectively. Before the N_2 adsorption/desorption testing, the samples were degassed at 150 ^oC under a vacuum condition for 12 h to remove adsorbed water and gas.

The small-angle X-ray scattering measurement (SAXS) was measured at the beamline I22 of Diamond Light source (Harwell, UK. Website: www.diamond.ac.uk/Instruments/Soft-Condensed-Matter/small-angle/I22) to further characterise the pore structures of carbon materials, followed

by the fitting of results based on the Porod method using Matlab.[7] The samples are filled into a Washer covered by two pieces of Scotch Magic tape, followed by mounting them into a sample grid (Figure S2g). The SAXS results have already removed the background.

X-ray photoelectron spectroscopy (XPS) was conducted to analyse the surface conditions and extrinsic defects of carbon materials using a Thermo Fisher K-Alpha* XPS facility with a monochromated Al-Kα X-ray source. The XPS results were fitted using the Avantage software. Before the XPS testing, carbon materials were placed onto the specific testing stage with a double-sided conductive carbon tape. The *ex-situ* XPS analysis was conducted to analyse the SEI components using the same Thermo Fisher K-Alpha* XPS facility with a monochromated Al-Kα X-ray source. Before the *ex-situ* XPS analysis, the one-step metallic deposition onto the carbon materials was performed at 1.0 mA cm^{-2} with a specific discharge capacity of 2.0 mAh cm^{-2} using a LAND CT 3001A battery testing system without any further cycling, thus ensuring the initial SEI undamaged. During the whole transfer process, a vacuum transfer capsule provided by Thermo Fisher was used to accommodate the samples, thus preventing surface contamination. XPS analysis of as-prepared sulfur cathode was conducted using the same facility.

X-ray diffraction (XRD) analysis was done to analyse the inner structures and intrinsic defects of carbon materials in a PANalytical X'Pert PRO with Cu-Kα source and the power setting of 40 mA and 40 kV power. The fitting of XRD patterns was done based on the Gaussian model. Before the XRD testing, carbon samples were loaded on a specific testing stage to ensure a flat surface.

3. Electrochemical Measurements

All the electrochemical measurements were conducted in stainless steel coin cells (CR2032, MTI Corporation) at room temperature, and all cell assembly procedures were done in an Argon-filled glove box (H_2O, O_2 < 0.5 ppm, mBraun). For the electrolytes, the solutions of 1 M $NaCF_3SO_3$ in ethylene carbonate-propylene carbonate (EC-PC, 1:1 v%, Sigma-Aldrich) mixed solvents, ethylene carbonate-diethyl carbonate (EC-DMC, 1:1 v%, Sigma-Aldrich) mixed solvents or diethylene glycol dimethyl ether (diglyme, Sigma-Aldrich) were used.

In the half cell configuration, sodium metal foil (8 mm in diameter, Alfa Aesar) was used as the counter electrode and the reference electrode at the same time. The carbon mat or other substrates (8 mm in diameter; Al, Ni, Cu and Sn, MTI Corporation; Graphite, Sigma-Aldrich; Carbon mats, Toray) was placed against metallic sodium with the same size, sandwiching the glass fibre membrane as the separator (16 mm in diameter, GF/D Glass microfibre filters, Whatman) soaked with 200 µL of electrolytes. The half cells were kept discharging (plating) and charging (stripping) at the current density of 1.0 mA cm^{-2} with a specific capacity of 2.0 mAh cm^{-2}. The maximum potential limitation of the half cells was set to be 1.5 V vs. Na^+/Na, while the corresponding minimum potential limitation was -5.0 V vs Na^+/Na.

In the symmetric cell configuration, two obtained Na/C composite electrodes or two bare metallic sodium foils were placed against each other, sandwiching the glass fibre membrane as the separator (16 mm in diameter, GF/D Glass microfibre filters, Whatman) soaked with 200 µL of electrolytes. The symmetric cells were kept discharging (plating) and charging (stripping) at different current densities including 0.1, 0.2, 0.5, 1.0 and 2.0 mA cm^{-2} for 0.5 h per (dis-)charge process, and were cycled at 1.0, 2.0 and 3.0 mA cm^{-2}. The maximum and minimum potential limitations of the symmetric cells were set to be 5.0 V and -5.0 V vs. Na^+/Na, respectively.

In the full cell configuration, the Na/C composite anode or bare metallic sodium foil (8 mm in diameter) was placed against the cathode with the same size, sandwiching the glass fibre membrane as the separator (16 mm in diameter, GF/D Glass microfibre filters, Whatman) soaked with 200 µL of electrolytes. For the full cells with Prussian blue cathode, the full cells were charged and discharged at 30, 60, 150, 300, 600 and 1200 mA g^{-1} between 2.0 to 4.2 vs Na^+/Na, and were cycled at 30 mA g^{-1} between 2.0 to 4.2 vs Na^+/Na. For the full cells with the sulfur cathode, the full cells were charged and discharged at 167.5 mA g^{-1} between 1.5 to 3.0 vs Na^+/Na.

All the galvanostatic charge/discharge (GCD) profiles and rate/cycling performance testing mentioned above were all achieved using the LAND CT 3001A battery testing system. The galvanostatic intermittent titration technique (GITT) testing was also conducted using the LAND CT 3001A battery testing system. The half cells of L700 were pre-discharged and charged at 1.0 mA cm^{-2} with the capacity of 2.0 mAh cm^{-2}, followed by the discharging of half cells using a pulse current at 1.0 mA cm^{-2} for 5 min and then a relaxation for 1 h until the potential went to the plating potential.

Electrochemical impedance spectroscopy (EIS) from 100 kHz to 0.01 Hz was measured on an Autolab PGSTAT204 electrochemical workstation and fitted using Zview. The EIS of half cells with different carbon mats in various electrolytes was measured at open circuit (around 2.5 V vs Na^+/Na), plated state at the first cycle (0 V vs Na^+/Na), stripped state at the first cycle (1.5 V vs Na^+/Na), plated state (0 V vs Na^+/Na) after 10 cycles, with a current density of 1.0 mA cm^{-2} and a specific capacity of 2.0 mAh cm^{-2}.

4. Theoretical modelling and simulations

All density functional theory (DFT) computations at the atomic level were performed with the aid of Gaussian 09 package.[8] Hybrid generalised gradient approximation (GGA) functional B3LYP[9, 10] was applied throughout the computation. The structure optimisation and subsequent vibrational analysis were carried out at the basis set level of 6-31G(d) with quadratic self-consistent field convergence criterion. The structures were shown in the figures with pyridinic, pyrrolic and quaternary nitrogen doping at different positions (i.e., centre and edges 1 to 3). A control group

without nitrogen doping (plain) was also considered. The binding energy was calculated according to the vibrational analysis results. The charge density and spin density were calculated under the scope of natural bond orbital (NBO)[11] analysis. The binding energies between the sodium atom and idealised graphene layer (E_b) were defined as follows:

$$E_b = E_{total} - E_{sub} - E_{Na}$$

where E_b, E_{sub}, E_{Na} were the energies of graphene layer models with sodium atom, pure graphene layer models, and a sodium atom in a sodium crystal, respectively.

The molecular level modelling of solvent molecules was conducted using ArgusLab based on the models of free EC, PC, DMC and diglyme solvent molecules. First, the standard models of solvent molecules with fixed bonding angles were built up. After that, the electrostatic mapping and the electron cloud distribution of HOMO/LUMO of a single molecule can be obtained from the software.

The macro-level finite element modelling was conducted using Ansys Maxwell to analyse the electric field distribution at the interface between electrolytes and electrodes during deposition. For the deposition onto the metallic sodium, two-dimensional models with the same surface morphology (only bulging nuclei) were firstly built up to compare the difference between the ester- and ether-based electrolyte. The ionic conductivities of the ester- and ether-based electrolyte were set to be 1.0 and 0.5 S m^{-1}, respectively. The length and height of the entire model were set to be 100 and 50 μm, respectively. The conductivity of metallic sodium was set to be 2.1 x 10^7 S m^{-1}. The overpotential of 0.1 V was utilised as the voltage excitation from the top edge of the electrolyte to the bottom edge of the electrode. The boundary of finite elements was set to be the Bolloon type during the simulation. Hence, the electric field and ion flux distribution during the deposition onto the metallic sodium can be obtained. Two-dimensional models with the different surface morphologies (bulging nuclei and concave nuclei) on the metallic sodium were also built up in the ether-based electrolyte for further comparison. For the deposition onto the carbon skeleton, three-dimensional models of carbon skeleton with nanofibre structures in the ether-electrolyte were built up as well. The conductivity of the carbon skeleton was set to be 10000 S m^{-1}. The length, width and height of the entire model were set to be 100, 50 and 50 μm, respectively. The overpotential of 0.1 V was utilised as the voltage excitation from the top face of the electrolyte to the bottom face of the electrode. The boundary of finite elements was set to be the Bolloon type during the simulation. Then, the three-dimensional electric field distribution and its differential vector profile of the deposition onto the carbon matrix can be obtained.

5. Numeric calculations and equations

For highly amorphous carbons, the intensity of G-peaks can be assumed to be a constant which is a representative of disorder parts as they are merely it is related to the stretching of sp^2 bonds. For very small L_a (< 2 nm), the strength of the D-mode is proportional to the number of benzene

rings in hard carbons indicating the ordered parts. The formula used to determine the average sizes of in-plane (L_a, nm) can be expressed as:[12]

$$L_a = \sqrt{5.4 \times 10^{-2} \times E_L^4 \times \frac{I_D}{I_G}} \quad \text{(S1)}$$

where E_L (=$\hbar\omega_L$, eV) is the laser excitation energy, and I_D/I_G is the intensity ratio of the D-peak and G-peak. For the light wavelength of 532 nm, E_L is 2.33 eV.

The average interlayer spacing d (Å) was calculated based on the Bragg formula as follows:[13]

$$d = \frac{\lambda}{2sin\theta} \quad \text{(S2)}$$

where θ (°) is the Bragg angle of peaks, and λ is the X-ray wavelength of 0.154 nm (1.54 Å).

A Porod method proposed by Stevens and Dahn was employed to analyse small-angle X-ray scattering (SAXS) data to probe the pore size of the carbon samples.[7] The equation for carbon materials with rich pore structures is presented as follows:

$$I(q) = \frac{A}{q^a} + \frac{B_1 a_1^4}{\left(1 + a_1^2 q^2\right)^2} + D \quad \text{(S3)}$$

where I(q) is the scattered intensity as a function of the scattering vector q, A is a scale factor for the surface scattering at low Q is proportional to the total surface area of large pores, B_1 is a scale factor for the pore scattering which is proportional to the total surface area of small pores. D is a constant background and a_1 is the characteristic length and associated with the radius of a spherical pore, by $R = a_1 \times \sqrt{10}$. This equation can be further modified by adding an a_1^2 term so that B_2 becomes proportional to the number of pores:[7]

$$I(q) = \frac{A}{q^a} + \frac{B_2 a_1^6}{\left(1 + a_1^2 q^2\right)^2} + D \quad \text{(S4)}$$

For carbon materials with intermediate-sized pores, an additional term can be added with a different characteristic length a_2. Then the equation becomes:

$$I(q) = \frac{A}{q^a} + \frac{B_3 a_2^6}{\left(1 + a_2^2 q^2\right)^2} + \frac{C a_3^6}{\left(1 + a_3^2 q^2\right)^2} + D \quad \text{(S5)}$$

where a_2 is the characteristic length of intermediate pores, C is a scale factor for the pore scattering proportional to the total surface area of intermediate pores.

Combined with GITT, the diffusion coefficient of Na^+ ions (D_{Na+}, $cm^2\ s^{-1}$) can be calculated based on Fick's second law:[14]

$$D_{Na^+} = \frac{4}{\pi\tau}\left(\frac{m_B V_m}{M_B S}\right)^2 \left(\frac{\Delta E_s}{\Delta E_\tau}\right)^2 \quad \text{(S6)}$$

where τ (s) is the pulse duration, m_B, M_B and V_M are the mass (g), the molar mass (g mol^{-1}) and the molar volume (mL mol^{-1}) of the active materials, and S is the active surface area (cm^2) of the working electrodes. ΔE_S (V) is the potential difference of two adjacent steady states, and ΔEτ (V) is the potential change owing to the pulse current.

According to typical Randles circuits, the Nyquist plot can be fitted:[15]

$$Z = R_s + \frac{1}{j\omega C_{dl} + \frac{1}{R_{ct1} + W_o}} + \frac{1}{j\omega C_l + \frac{1}{R_{leak}}} \quad \text{(S7)}$$

$$Z = R_s + \frac{1}{j\omega C_{dl} + \frac{1}{R_{ct1}}} + \frac{1}{j\omega C_{dl} + \frac{1}{R_{ct2} + W_o}} + \frac{1}{j\omega C_l + \frac{1}{R_{leak}}} \quad \text{(S8)}$$

$$Z = R_s + \frac{1}{j\omega C_{dl} + \frac{1}{R_{ct1}}} + \frac{1}{j\omega C_{dl} + \frac{1}{R_{ct2}}} + \frac{1}{j\omega C_{dl} + \frac{1}{R_{ct3} + W_o}} + \frac{1}{j\omega C_l + \frac{1}{R_{leak}}} \quad \text{(S9)}$$

where Z (Ω) is the impedance, R_s (Ω) is the inner resistance, R_{ct} (Ω) is the charge-transfer resistance. The sum of R_s and R_{ct} is the equivalent series resistance (**ESR**) of the device. Furthermore, C_{dl}, C_l, W_o and R_{leak} respectively represent the double-layer capacitance, the low-frequency mass capacitance, the Warburg element and the low-frequency leakage resistance. All the equivalent circuits inserted in Figure 4g are simplified to mainly focus on the ESR part, thus facilitating the following discussion on the interface conditions at different states. At the low-frequency region (close to 0.01 Hz), processes like ion diffusion with relatively slow dynamics can be detected. In the high-frequency region (close to 100 kHz), processes like ion reaction and migration with relatively faster dynamics can be discovered. At the maximum frequency (starting point of the semicircle), the electron migration with the fastest dynamic can be measured.

The charge/discharge specific capacity values of the working electrodes were calculated from GCD according to Equation S8 as follows:[16]

$$Q_{electrode} = \frac{I\Delta t}{3.6m} \quad \text{(S10)}$$

where $Q_{electrode}$ (mAh g^{-1}) is the charge/discharge specific capacity. I (A) is the constant charge/discharge current, ΔU (=U_{max}-IR_{drop}-U_{min}, V) is the working voltage window, m (g) is the active mass on the working electrodes, and Δt (s) is the charge/discharge time.

The power/energy density values of the full cells were obtained using Equation S9 and S10, respectively, as follows:

$$E_{device} = \frac{I}{3.6M}\int_{t_1}^{t_2} U(t)dt \quad \text{(S11)}$$

$$P_{device} = \frac{3600E}{\Delta t} \quad \text{(S12)}$$

where E_{device} (Wh kg^{-1}) is the energy density of devices, and P_{device} (W kg^{-1}) is the power density. I (A) is the constant charge/discharge current, M (g) is the total mass of active materials in both anodes and cathodes, and Δt (s) is the charge/discharge time. U(t) (V) is the voltage that changes with time under galvanostatic discharging or charging, t_1 (s) is the start time of charge/discharge processes, and t_2 (s) is the end time.

Results and discussion

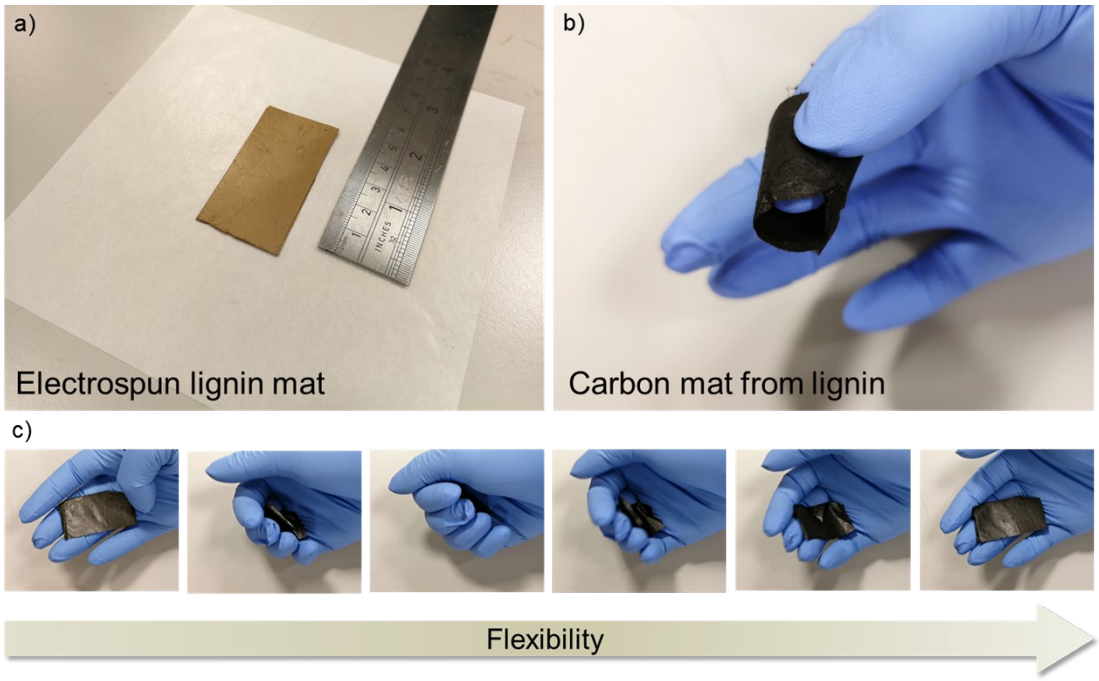

Figure S1. a) The photograph of a piece of electrospun lignin mat and b) a non-woven fabric piece of carbonised skeletons. c) Demonstration of the flexibility of lignin-derived carbon mats by bending and releasing.

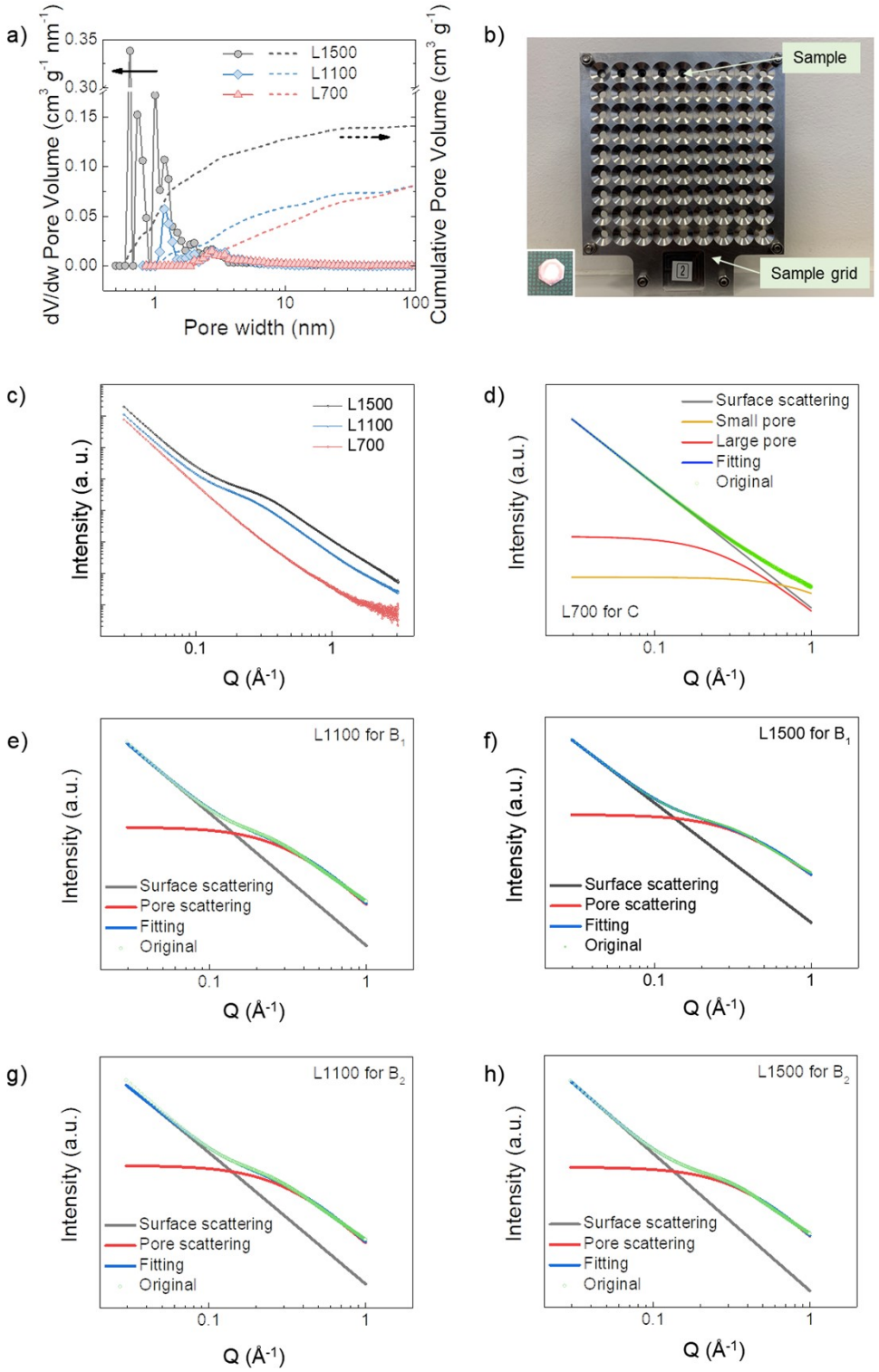

Figure S2. a) The pore size distribution based on the non-local density functional theory (NLDFT) method L700, L1100 and L1500; b) The photograph of sample grid for SAXS measurement with an inserted photograph of a washer used to fix the samples. c) The small-angle X-ray scattering (SAXS) patterns of L700, L1100 and L1500; d) Fitted SAXS patterns of L700 based on Equation S5 for the value of C; Fitted SAXS patterns of e) L1100 and f) L1500 based on Equation S3 for the value of B_1; Fitted SAXS patterns of g) L1100 and h) L1500 based on Equation S4 for the value of B_2; (The SAXS

results have already removed the background)

The SAXS pattern of L700 shows the negligible pore structures of L700.[7] Furthermore, the SAXS patterns of L1100 and L1500 can be fitted based on Equation S3 and S4, while the SAXS pattern of L700 can be fitted based on Equation S5. B_1 for L1100 and L1500 is a scale factor for the pore scattering which is proportional to the total surface area of small pores, while C for L700 is a scale factor for the pore scattering proportional to the total surface area of intermediate pores. B_2 becomes proportional to the number of pores.[17] According to these results, with the increase of carbonisation temperatures, the pore structures in carbon skeletons including the total surface area of pores and the number of pores increase. This trend is consistent with the conclusions from N_2 adsorption and desorption results.

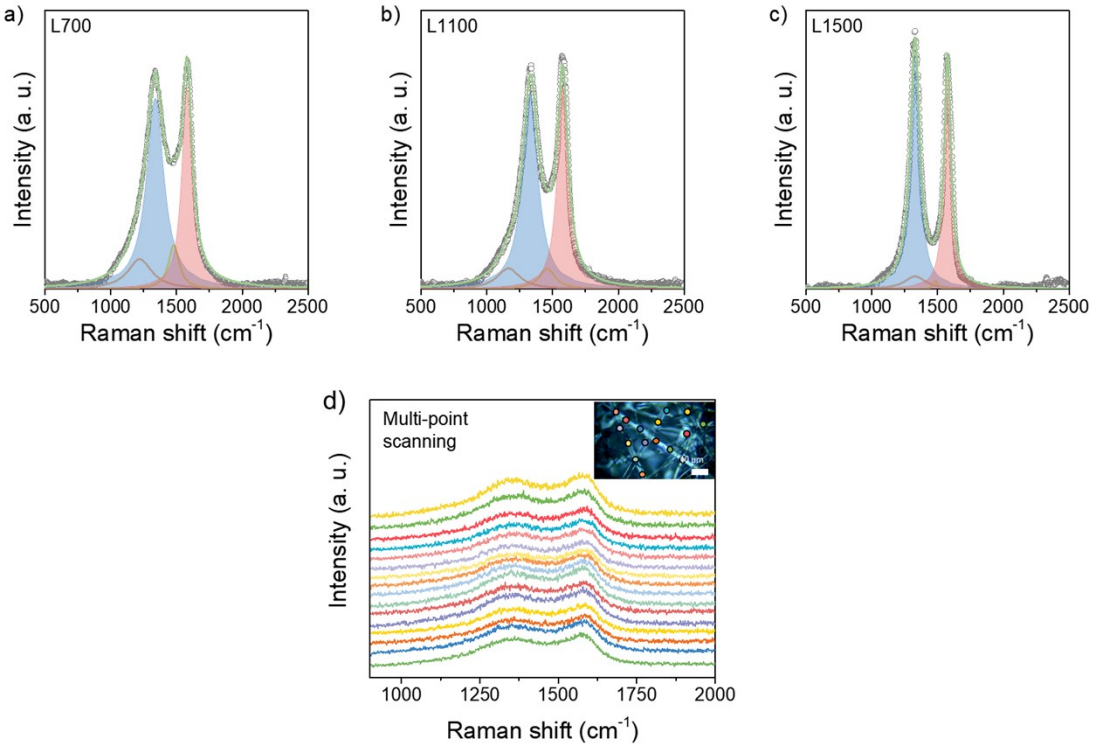

Figure S3. Fitted Raman spectra of a) L700, b) L1100 and c) L1500 using the Lorentzian methods; d) Raman spectra of an area of L700 through the multi-point scanning model, which is conducted to further prove the uniformity of defect sites of L700. With the uniformly distributed defect sites, L700 can prevent the dendrite growth as a protection skeleton for sodium metal anodes.

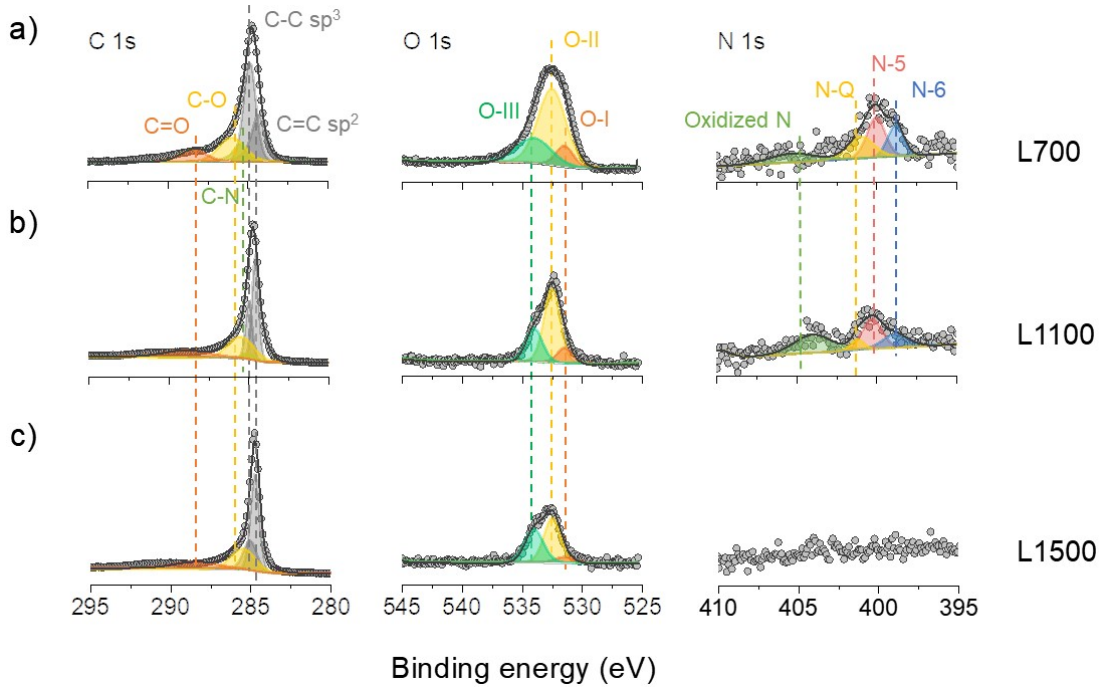

Figure S4. Fitted C 1s, N 1s and O 1s core-level XPS spectra of a) L700, b) L1100 and c) L1500

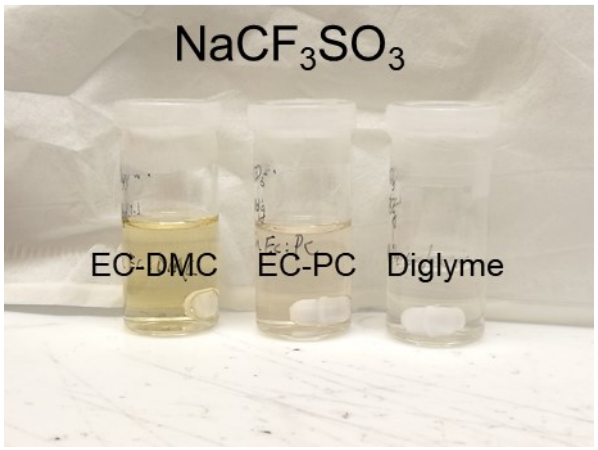

Figure S5. The photograph of $NaCF_3SO_3$ in EC-DMC, EC-PC or diglyme

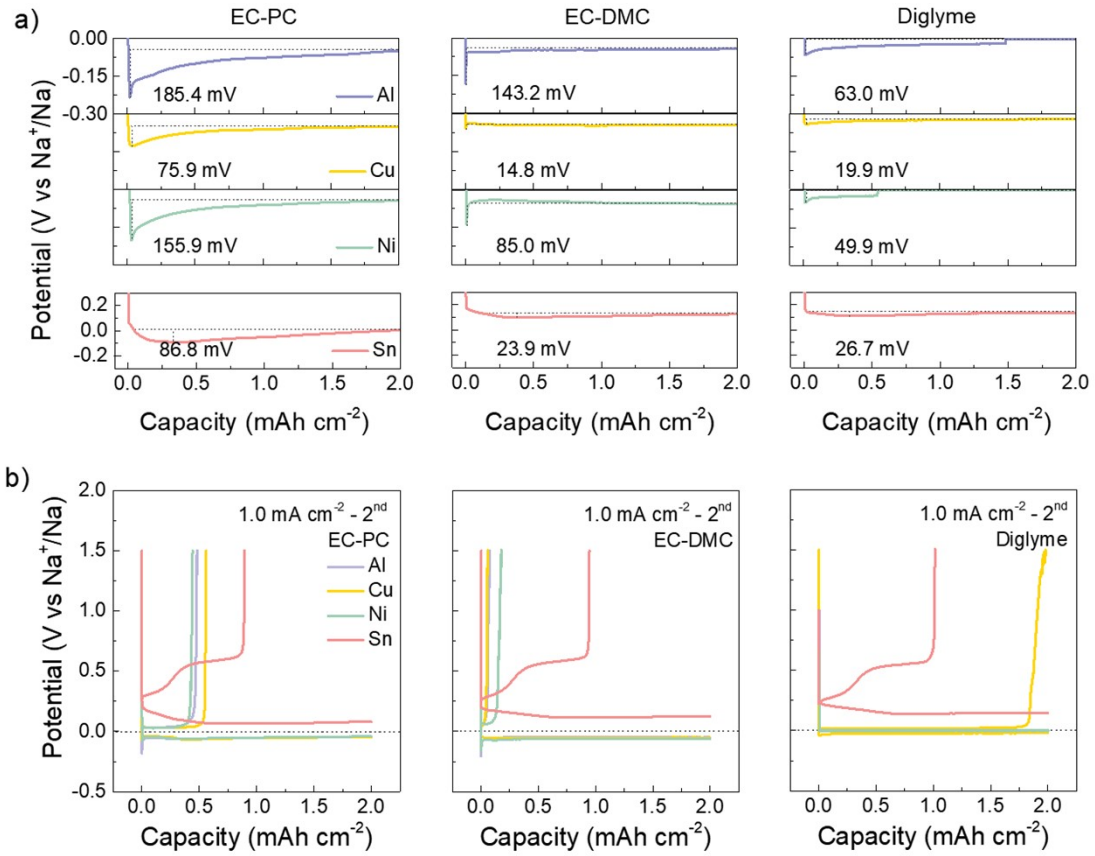

Figure S6. a) The potential-capacity profiles (the 1st cycle) showing initial nucleation overpotentials of sodium deposition on Al, Cu, Ni and Sn at 1 mA cm^{-2} using 1 M $NaCF_3SO_3$ in EC-PC (left), EC-DMC (middle) or diglyme (right); b) The specific GCD curves (the 2nd cycle) of sodium plating/stripping on Al, Cu, Ni and Sn at 1mA cm^{-2} using 1 M $NaCF_3SO_3$ in EC-PC (left), EC-DMC (middle) or diglyme (right).

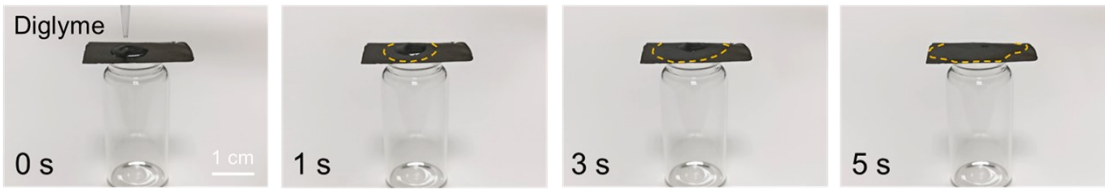

Figure S7. The wettability testing of L700 with diglyme, where the 100μL diglyme can be fully absorbed in a piece of L700 since no diglyme can penetrate the L700.

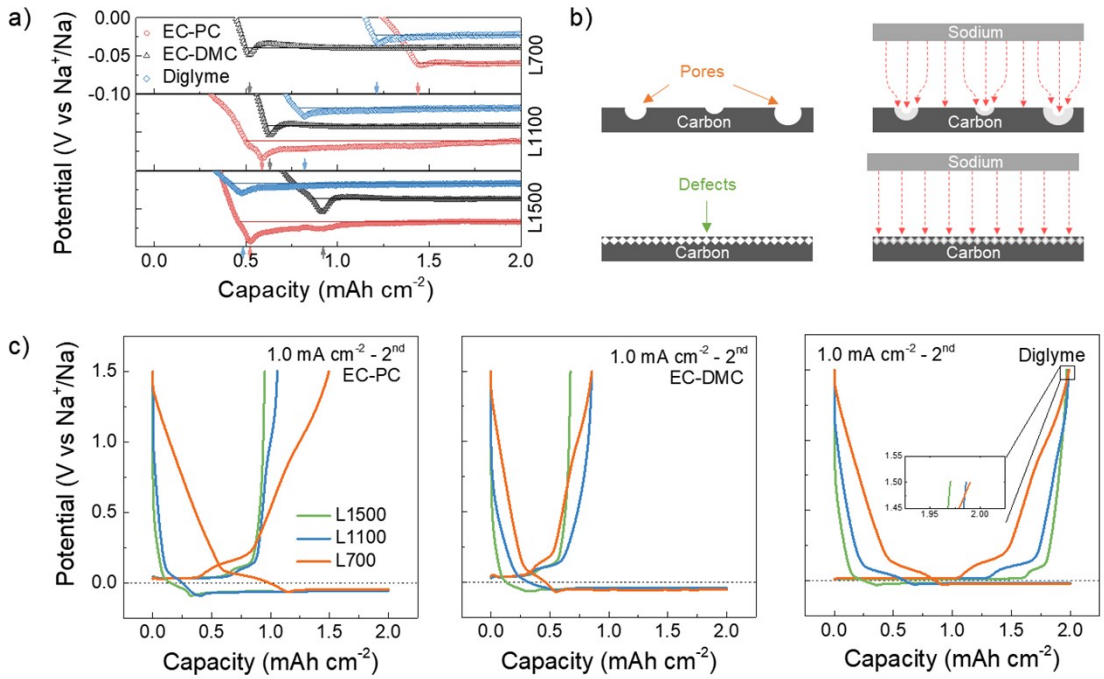

Figure S8. a) The potential-capacity profiles (the 1st cycle) at 1 mA cm^{-2} showing initial nucleation overpotentials of sodium deposition on L700, L1100 and L1500 using 1 M $NaCF_3SO_3$ in EC-PC, 1 M $NaCF_3SO_3$ in EC-DMC or 1 M $NaCF_3SO_3$ in diglyme, respectively; b) Schematic illustration of ion flux distribution and metallic deposition on the carbon with pore structures or defect structures; c) GCD curves (the 2nd cycle) of metallic sodium plating/stripping at 1mA cm^{-2} on L700, L1100 and L1500 using 1 M $NaCF_3SO_3$ in EC-PC, 1 M $NaCF_3SO_3$ in EC-DMC or 1 M $NaCF_3SO_3$ in diglyme, respectively.

As illustrated in Figure S8b, the metallic deposition induced by pore structures on the surface of carbon materials is uneven because the pore structures cause the non-uniform ion flux distribution, which can also be proven by the finite element simulation results. In comparison, the metallic deposition induced by defect structures is more homogenous with a uniform ion flux distribution. In Figure S8a and b, the irreversible capacity can be observed in the ester-based electrolyte because of the repeated fragmentation and reconstruction of unstable solid electrolyte interphase (SEI) and the formation of "dead" sodium during cycling, but L700 still has the best reversibility compared with L1100 and L1500, which further proves the defect structures are more beneficial to the metallic deposition behaviours than pore structures.

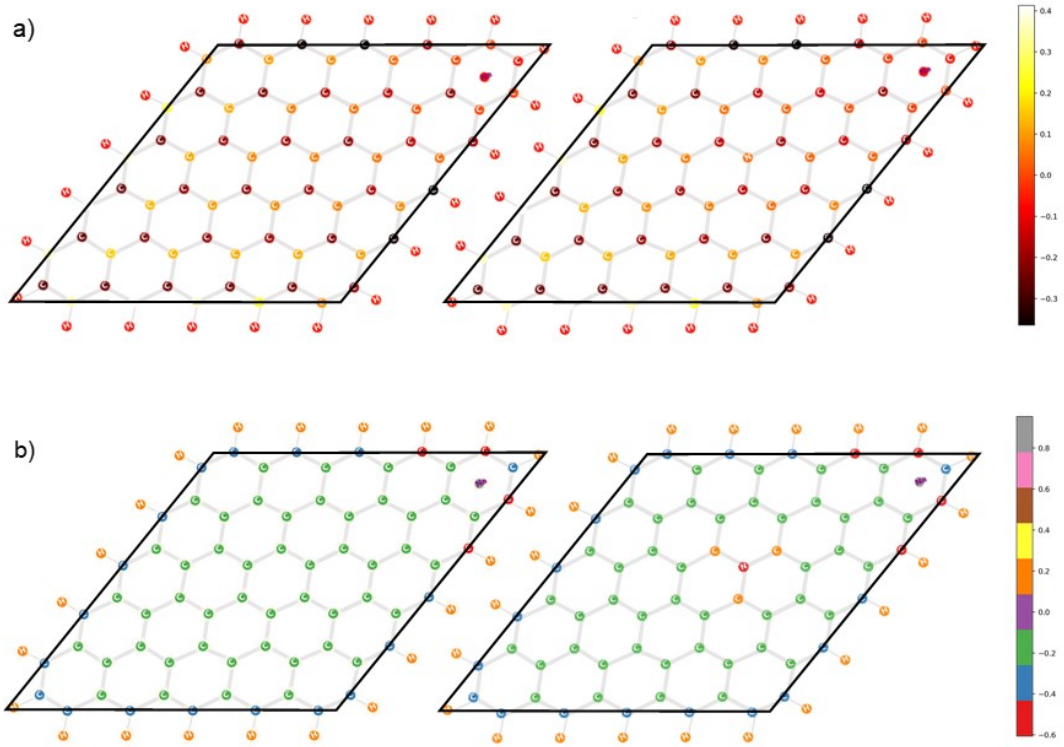

Figure S9. a) Left: Spin densities between sodium atoms and L1500 with intact graphene layers, Right: Spin densities between sodium atoms and L700 with quaternary nitrogen-doped graphene layers; b) Left: Local charge densities between sodium atoms and L1500 with intact graphene layers, Right: the local charge densities between sodium atoms and L700 with quaternary nitrogen-doped graphene layers.

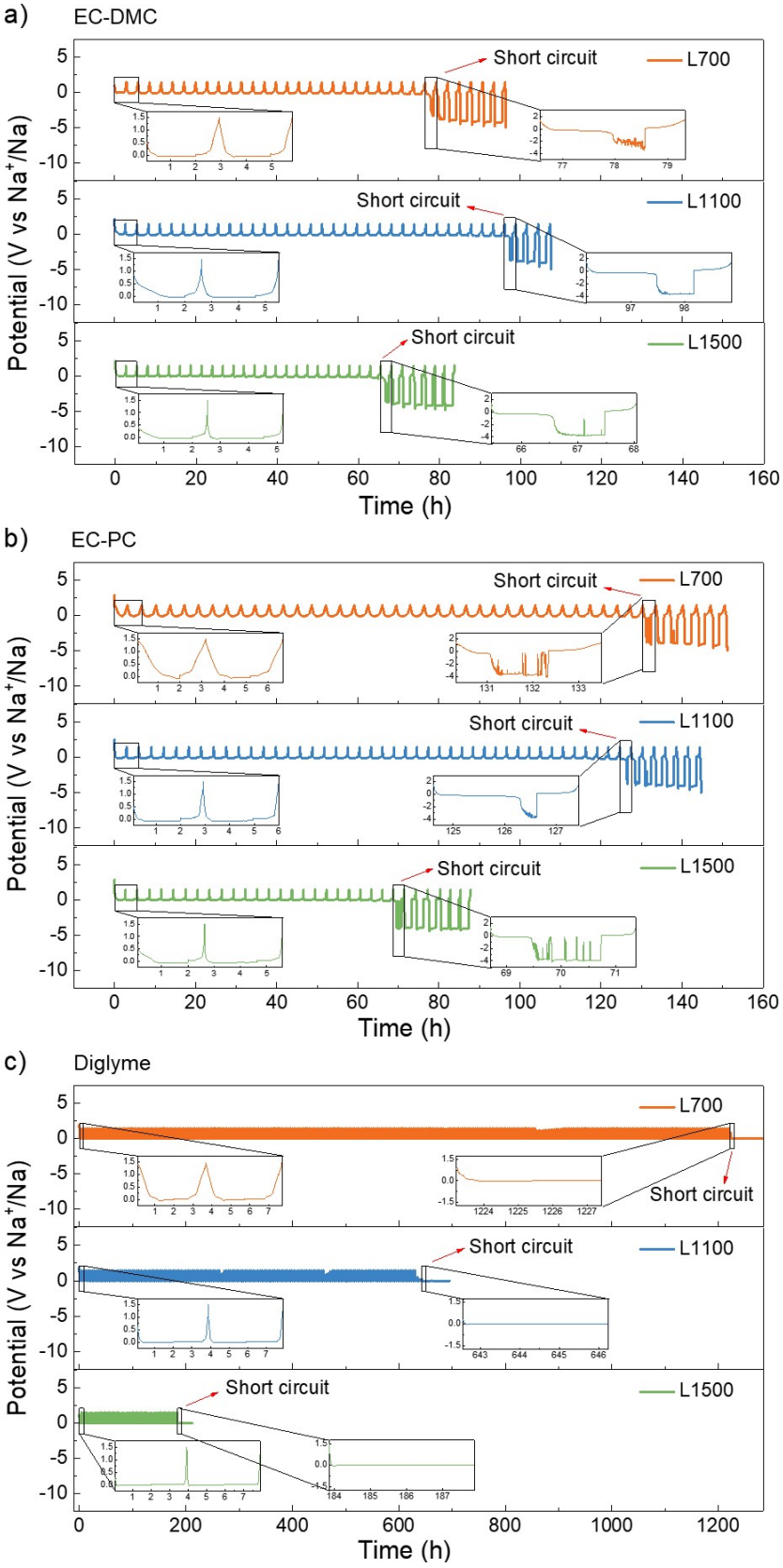

Figure S10. The GCD of the plating/stripping of metallic sodium onto/from L700, L1100 and L1500 using 1 M $NaCF_3SO_3$ in a) EC-DMC, b) EC-PC or c) diglyme, respectively. The defective structures of L700 can also obviously reduce the polarisation phenomenon including the IR_{drop} of sodium plating and stripping, indicating the enhanced interface contact between metallic sodium and L700.

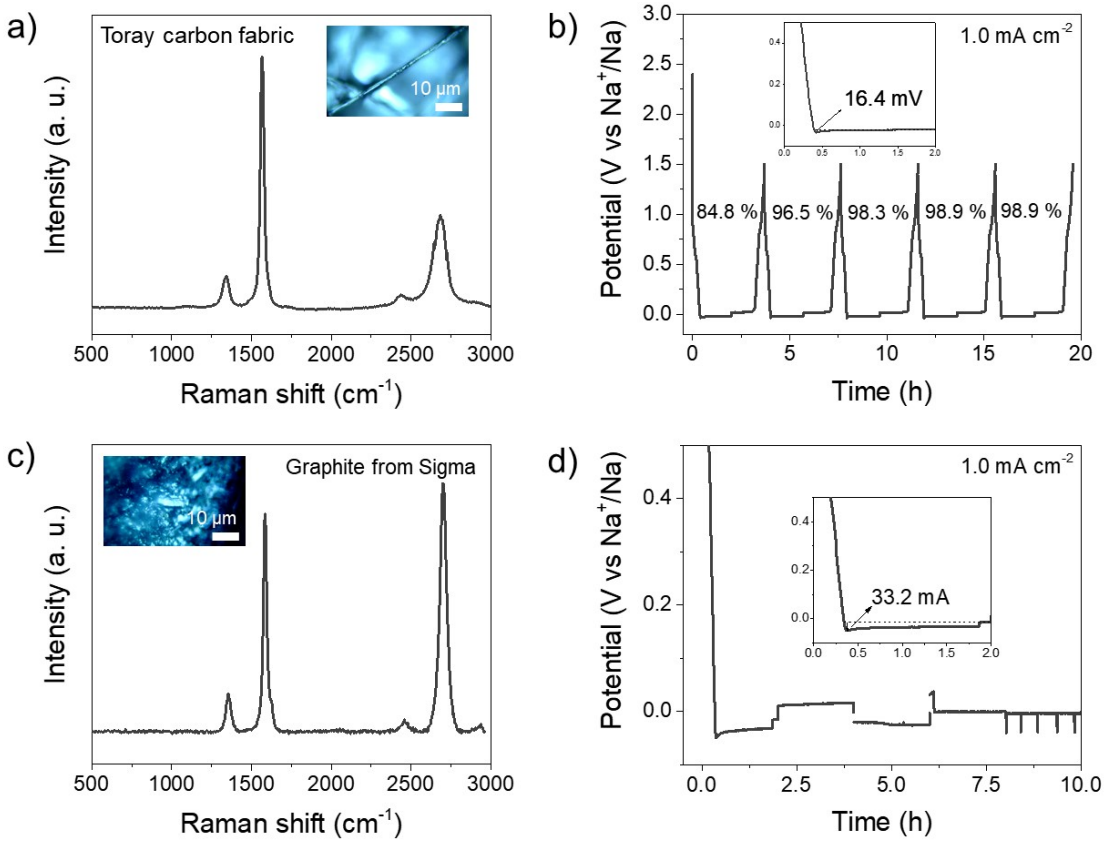

Figure S11. a) Raman spectrum of carbon mats from Toray with the inserted photography of the sample; b) The charge-discharge curves of carbon mats from Toray in the half cell configuration for sodium plating and stripping using 1 M $NaCF_3SO_3$ in diglyme; c) Raman spectrum of commercial graphite substrate from Sigma-Aldrich with the inserted photography of the sample; b) The charge-discharge curves of commercial graphite substrate from Sigma-Aldrich in the half cell configuration for sodium plating and stripping using 1 M $NaCF_3SO_3$ in diglyme.

We have applied carbon mats from Toray (www.alfa.com/en/catalog/045356/) and commercial graphite from Sigma-Aldrich (www.sigmaaldrich.com/GB/en/product/aldrich/282863) and which both feature negligible defects and few pores as the comparison samples in sodium metal batteries. Please see Figure S11a and c of Raman spectra as the proofs of the highly ordered structures of carbon mats and graphite. In Figure S11 b and d, we can see that the initial overpotentials of Toray carbon fabric and graphite are 16.4 and 33.4 mV, respectively, which are much larger than that of L700 (10.6 mV) with rich defects and negligible pores in the same electrolyte. The corresponding reversibility and efficiencies are obviously worse than those of L700 as well, where efficiencies of L700 are all over 99.0% starting from the second cycles. Combined with the comparison of our carbon mats to commercial defect-free carbon samples, we can further prove that defects play a beneficial role when metallic sodium deposits onto carbon materials.

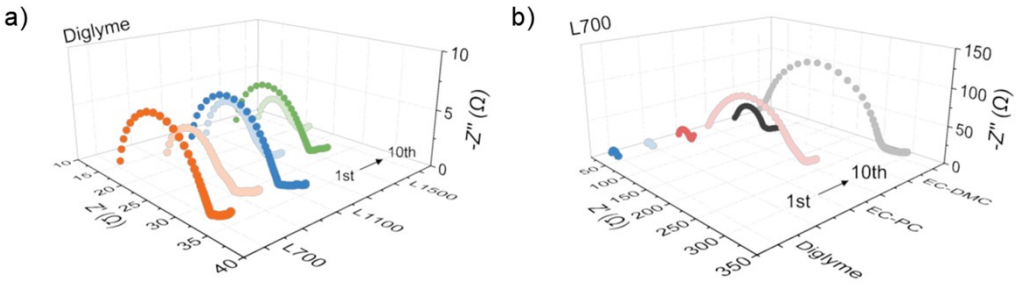

Figure S12. a) EIS plots of L700, L1100 and L1500 using 1 M $NaCF_3SO_3$ in diglyme before and after cycling; b) EIS plots of L700 using 1 M $NaCF_3SO_3$ in diglyme, 1 M $NaCF_3SO_3$ in EC-PC or 1 M $NaCF_3SO_3$ in EC-DMC before and after cycling.

The comparison of EIS with different carbon skeletons and electrolytes at plated states before and after cycling is also conducted (Figure S11). When the same substrate (L700) is employed, the charge transfer resistance in ester-based electrolytes is smaller than that in the ether-based electrolyte at the beginning, which means the initial ionic conductivity of the ether-based electrolyte is lower. This result can be consistent with the finite element simulation exhibited before. However, after cycling, the charge transfer resistance in ester-based electrolytes significantly increases, while in the ether-based electrolyte, the charge transfer resistance decreases. This phenomenon further indicates the difference between ester- and ether-based electrolytes in the stability and ionic conductivity of intermediate phases formed during cycling.

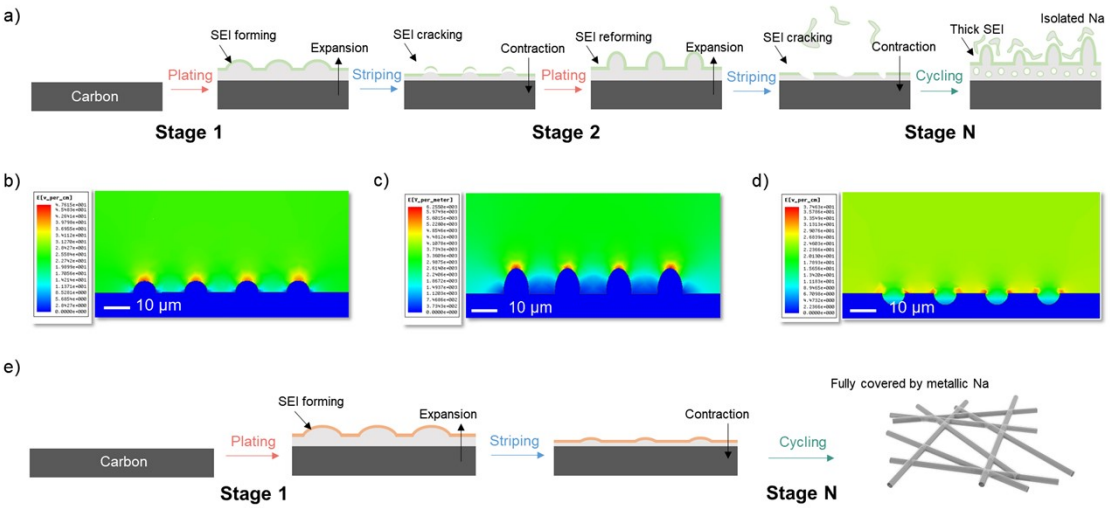

Figure S13. a) Schematic illustration of the sodium stripping and plating process in EC-PC or EC-DMC. Stage 1: The SEI forms and Na^+ ions insert into the carbon skeleton above 0 V vs Na^+/Na, while the metallic sodium keeps plating onto the carbon skeleton below 0 V vs Na^+/Na; Stage 2: The volume change caused by sodium plating and striping makes the SEI crack, followed by the reformation of the SEI. Afterwards, the uneven plating results in Na dendrites; Step N: sodium stripping isolates sodium dendrites into electrolytes. b-c) Finite element modelling of the electric fields in different stages of sodium plating and striping, which proves the rough surface can induce uneven current flows. e) Schematic illustration of the sodium stripping and plating process in diglyme, which is more uniform.

The reasons for cell fading in ester- and ether-based electrolytes differ. In EC-DMC and EC-PC, the SEI is unstable because a large number of inorganic components exists in SEI as described in the main text. During plating/stripping of metallic sodium, the large volume change of metallic sodium on carbon skeletons makes the SEI keep cracking and reforming. The rough surface caused by the reformation of the SEI would induce the uneven sodium plating and then form sodium dendrites. Importantly, the sodium dendrites would further induce the uneven sodium plating. Finally, the isolated sodium layers rapidly form above the thick SEI of active metallic sodium, thus totally changing the plating and striping behaviours on the substrate (Figure S12 a and b). The SEI in diglyme, however, is more flexible and stable than that in carbonate-based electrolytes because of the continuous organic phase of the SEI in diglyme. In comparison to the plating and striping behaviours in EC-DMC and EC-PC, the metallic sodium can be plated and stripped uniformly during cycling without the endless reconstruction of the SEI. Only a few irreversible metallic sodium remains on the defect sites and surface of carbon skeletons because of the average Coulombic efficiency of 99.6%. After ultra-long cycling, the active sites are fully occupied by irreversible metallic sodium, followed by the plating of metallic sodium on the irreversible metallic sodium instead of active sites on carbon skeletons, thus changing the GCD curves in the end (Figure S10c).

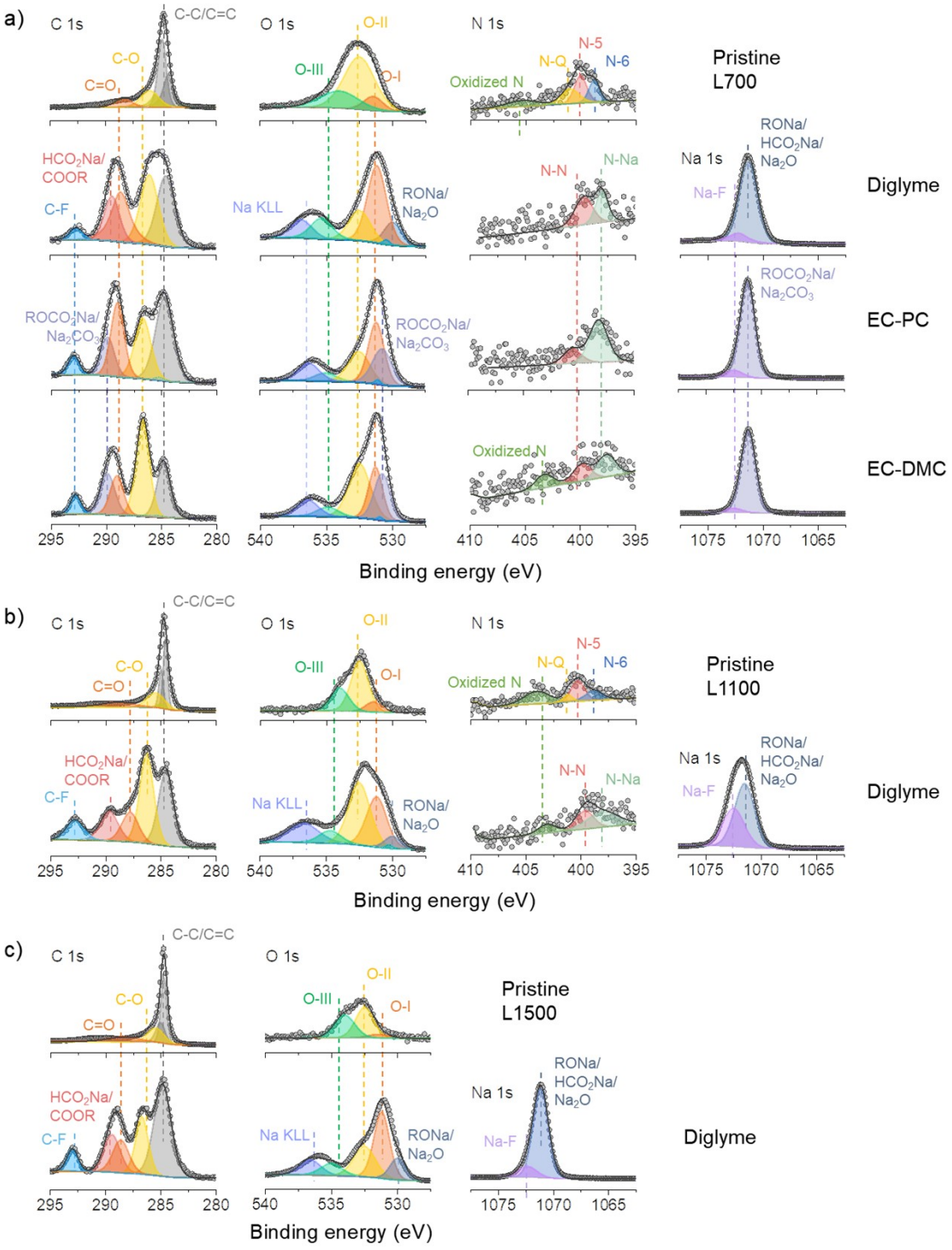

Figure S14. a) Fitted C 1s, O 1s, N 1s and Na 1s core-level XPS spectra of pristine L700, plated L700 using 1 M $NaCF_3SO_3$ in diglyme, plated L700 using 1 M $NaCF_3SO_3$ in EC-PC, and plated L700 using 1 M $NaCF_3SO_3$ in EC-DMC after the first cycle of metallic deposition at 1.0 mA cm^{-2} with a specific discharge capacity of 2.0 mAh cm^{-2}; b) Fitted C 1s, O 1s, N 1s and Na 1s core-level XPS spectra of pristine L1100, plated L1100 using 1 M $NaCF_3SO_3$ in diglyme after the same deposition process; c) Fitted C 1s, O 1s and Na 1s core-level XPS spectra of pristine L1500, plated L1500 using 1 M $NaCF_3SO_3$ in diglyme after the same deposition process.

In our study, all the SEI layers from the decomposition of the three electrolytes showed fluorinated interfaces. The fluorinated composition in SEI layers can improve the interface stability due to their strong electron-withdrawing property for tuning the electron density and frontier molecular orbitals of the SEI layers.[18, 19]

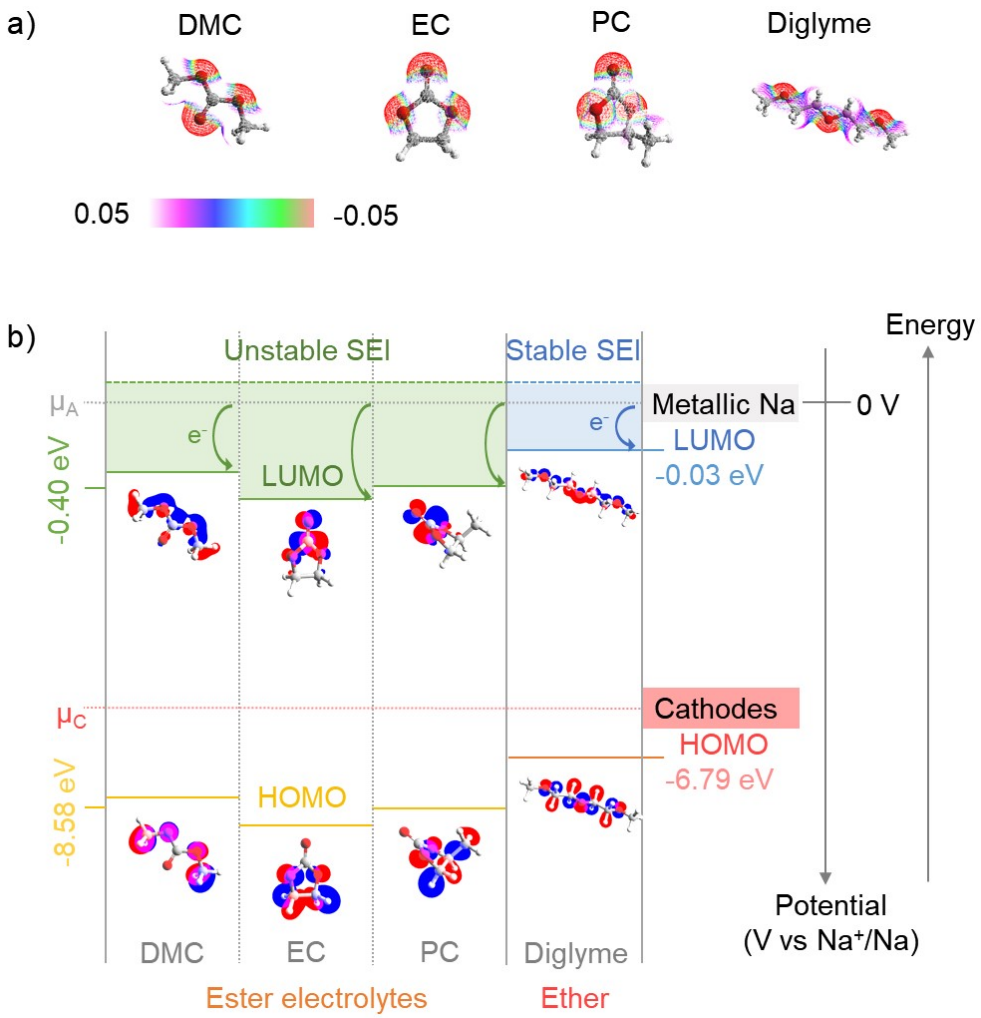

Figure S15. a) The electrostatic potential maps of DMC, EC, PC and diglyme (Red colour means the negative charge, and white colour means the positive charge); b) Schematic illustration of energy states of electrodes, ester-based electrolytes and ether-based electrolytes, where the lowest unoccupied molecular orbital (LUMO), the highest occupied molecular orbital (HOMO) levels and their corresponding electron cloud distribution of free electrolyte solvent molecules (i.e., DMC, EC, PC and diglyme) are presented as well.

When the energy level (μ_A, chemical potential) of metallic sodium is higher than the LUMO of solvent molecules, the electrons can transfer from μ_A of metallic sodium to the LUMO of solvent molecules, thus reducing the electrolyte to decompose and form a passivation solid electrolyte interphase (SEI) layer on the surface of metallic sodium as a barrier to block the further transfer of an electron from μ_A of metallic sodium to the LUMO of solvent molecules.[20]

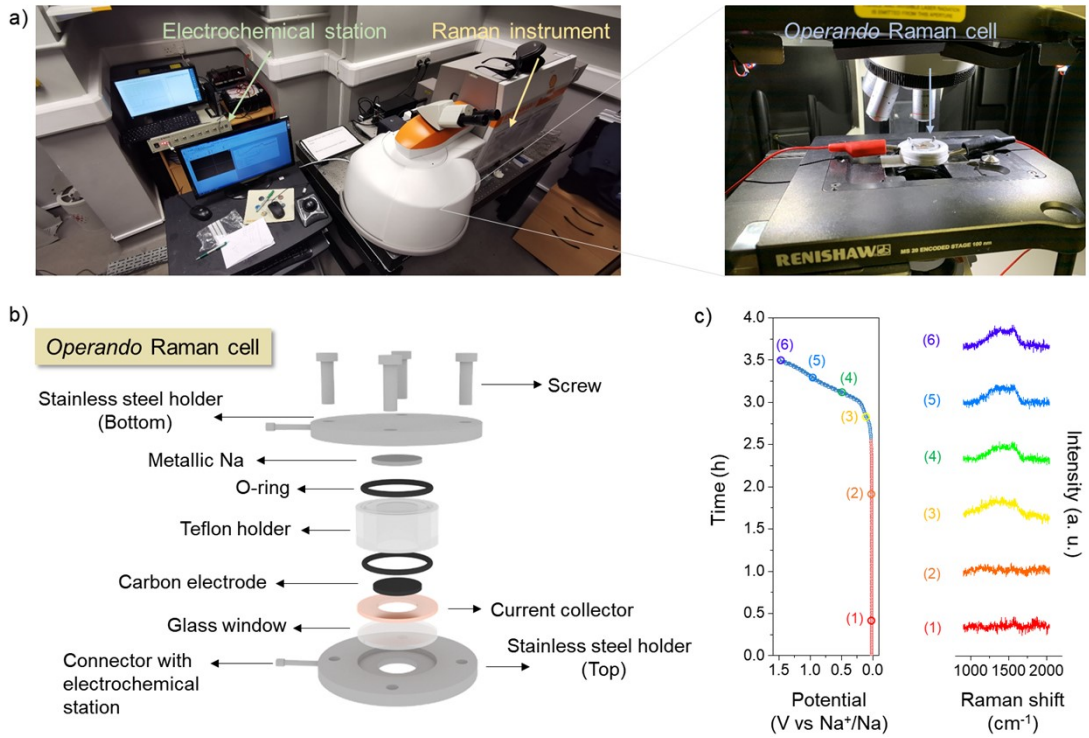

Figure S16. a) The photograph of *operando* Raman measurement; b) The configuration of the *operando* Raman cell; c) Raman spectra of L700 during the first stripping process in 1 M $NaCF_3SO_3$ in diglyme (right), with the corresponding plating electrochemical curve (left) at 0.5 mA cm^{-2}.

L700 has exhibited the largest sloping capacity (i.e., insertion capacity) because of its abundant defects. In the half cell, the capacity can be categorised as the insertion capacity when the working potential is above 0 vs Na^+/Na. When the working potential is below 0 vs Na^+/Na, the deposition of metallic sodium onto the carbon mat happens, leading to the plating capacity in the charge-discharge curves of half cells. The insertion of sodium ions into carbon materials can be facilitated by defective structures. After that, the sodiophilic properties of carbon materials can be further enhanced because Na^+ ions exist in their structures. Therefore, the larger insertion capacity can contribute to the better durability of L700 for sodium plating and stripping in the half cells. In addition, the insertion reactions are highly reversible since the sloping capacity can be observed from each charge-discharge curve of half cells.

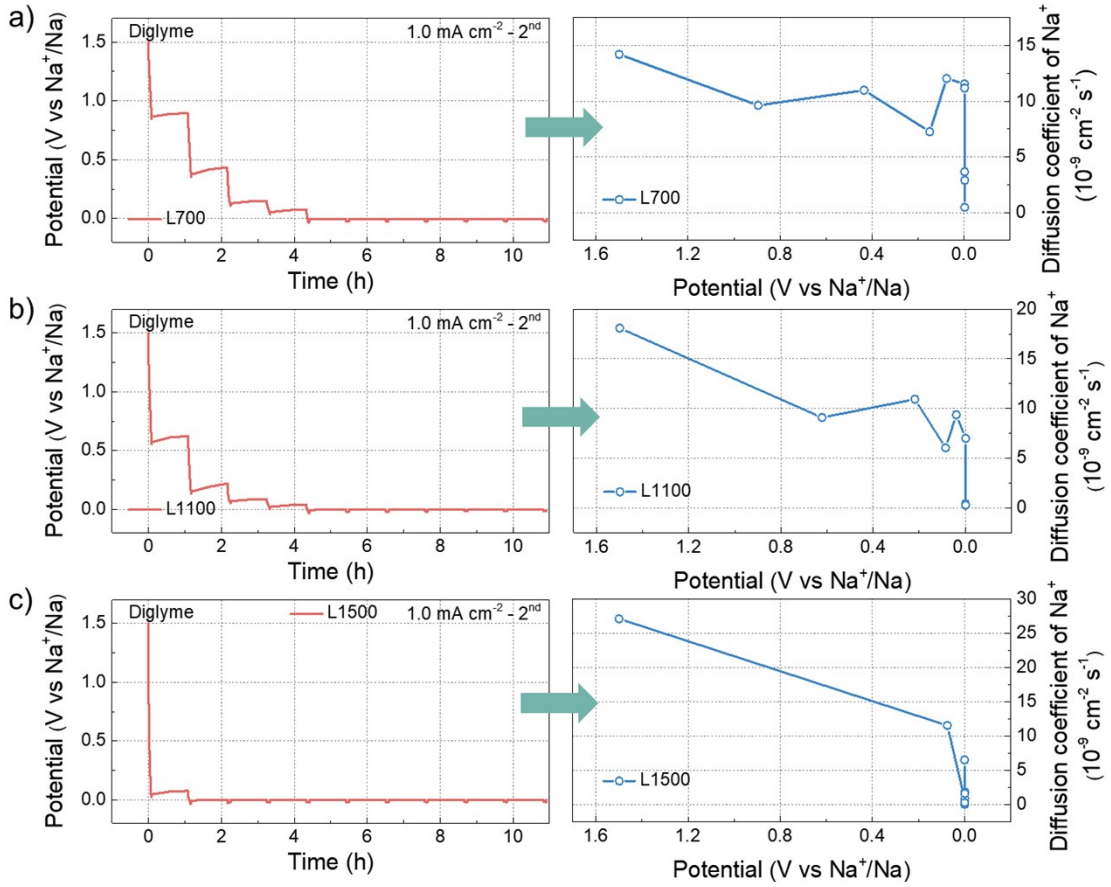

Figure S17. GITT profiles of a) L700, b) L1100 and c) L1500 using 1 M $NaCF_3SO_3$ in diglyme (left) and their calculated diffusion coefficient of Na^+ ions (right).

As we can see from the GITTs, the insertion behaviour possesses a higher average diffusion coefficient than the plating process, representing a faster kinetic of the insertion behaviour. When the potential enters the region of the plating process, the corresponding diffusion coefficient rapidly decreases. Compared with L1100 and L1500, the diffusion coefficients of L700 exhibits a lower decrease rate because of the larger insertion capacity. Therefore, combining the material characterisations of L700, L1100 and L1500, we can conclude that the existence of rich defects in L700 can significantly contribute to the larger insertion capacity rather than the abundant pores in L1500, which is identical to our explanation on *operando* Raman spectra at the sloping region of sodiation (> 0.1 V vs Na^+/Na). Meanwhile, the insertion behaviour at the defect sites with a faster kinetic than plating process can be further confirmed.

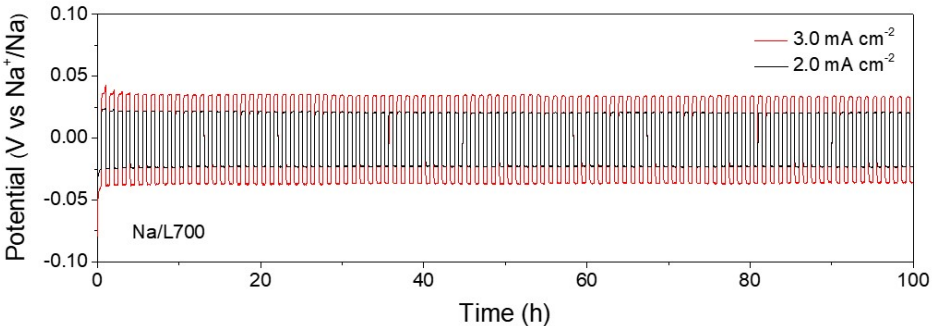

Figure S18. Cycling stability of Na/L700 composite anodes in the symmetrical cell at current densities of 2.0 and 3.0 mA cm^{-2} with a specific capacity of 1.0 and 1.5 mAh cm^{-2}, respectively, using 1 M $NaCF_3SO_3$ in diglyme.

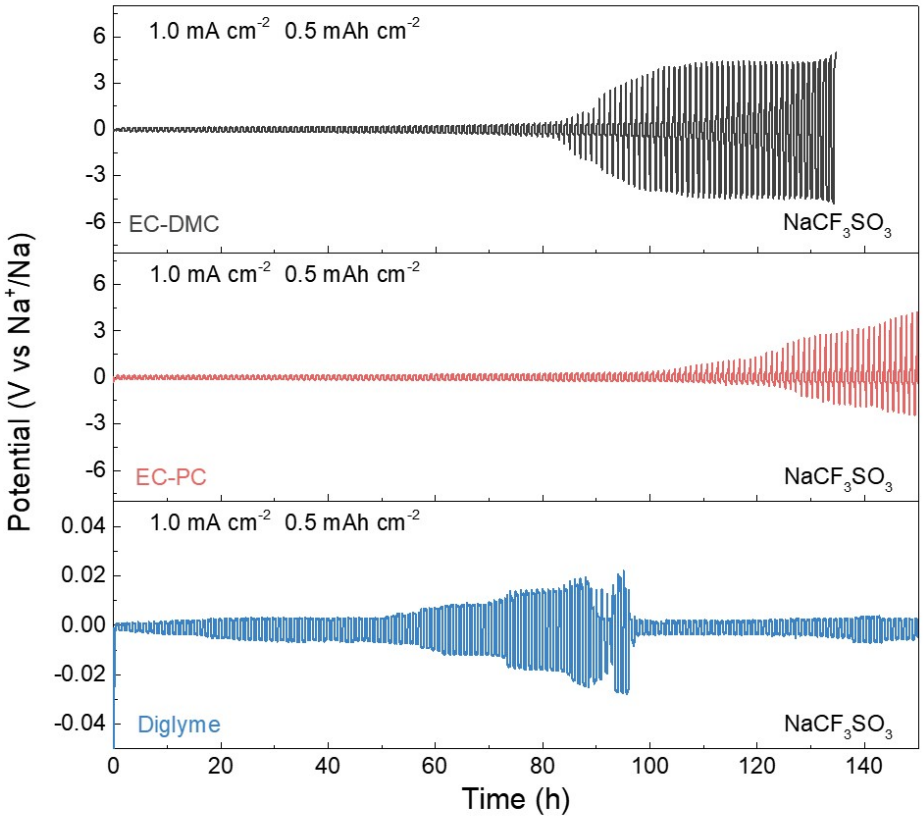

Figure S19. The potential hysteresis of the plating and stripping of bare metallic sodium symmetric cells using 1 M $NaCF_3SO_3$ in EC-DMC, 1 M $NaCF_3SO_3$ in EC-PC and 1 M $NaCF_3SO_3$ in diglyme during cycling at 1.0 mA cm^{-2} with a specific capacity of 0.5 mAh cm^{-2}.

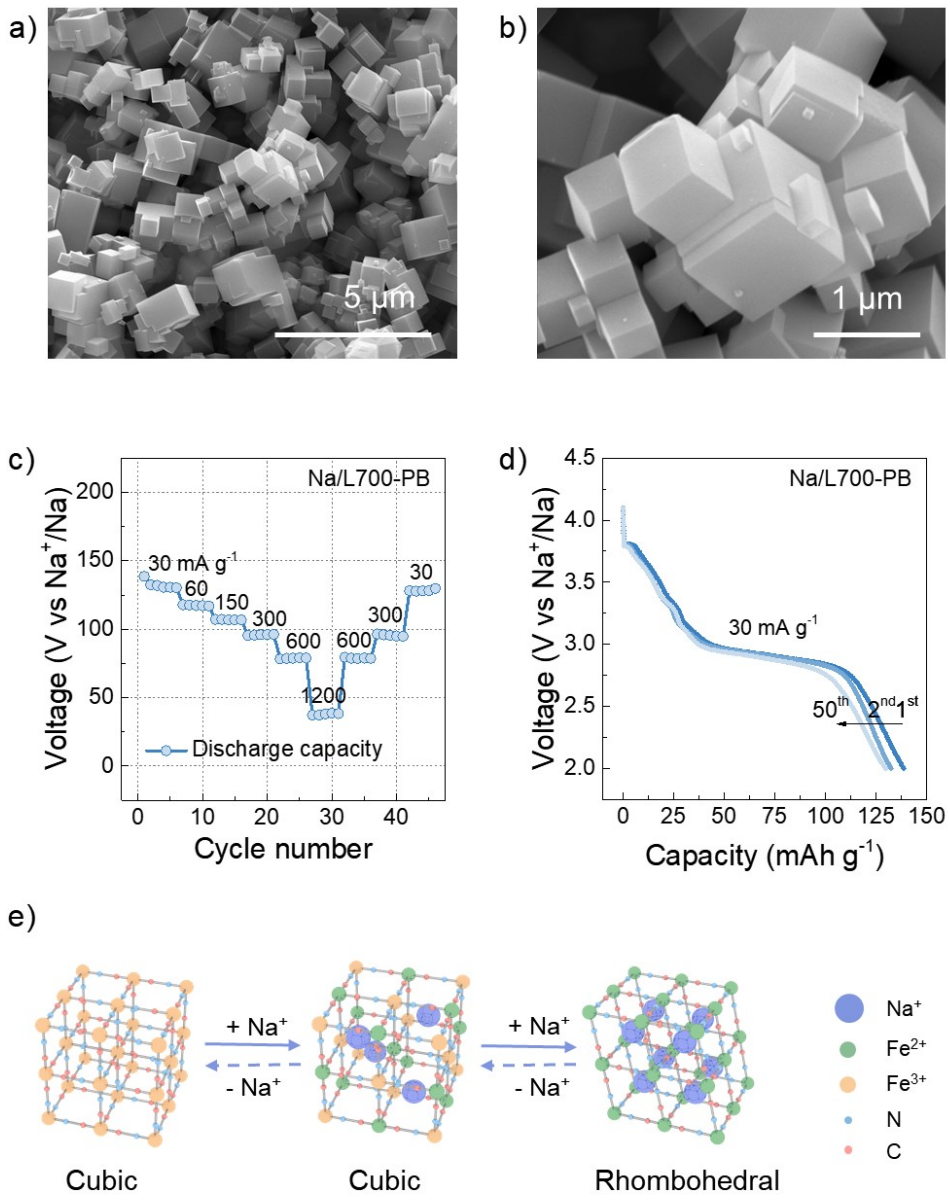

Figure S20. a) and b) SEM images of synthesized Prussian blue; c) Rate performance and d) cycling performance of sodium metal batteries with the Prussian blue cathode; e) Schematic illustration of the Na^+ ion storage mechanism of Prussian blue $Fe^{III}Fe^{III}(CN)_6$.

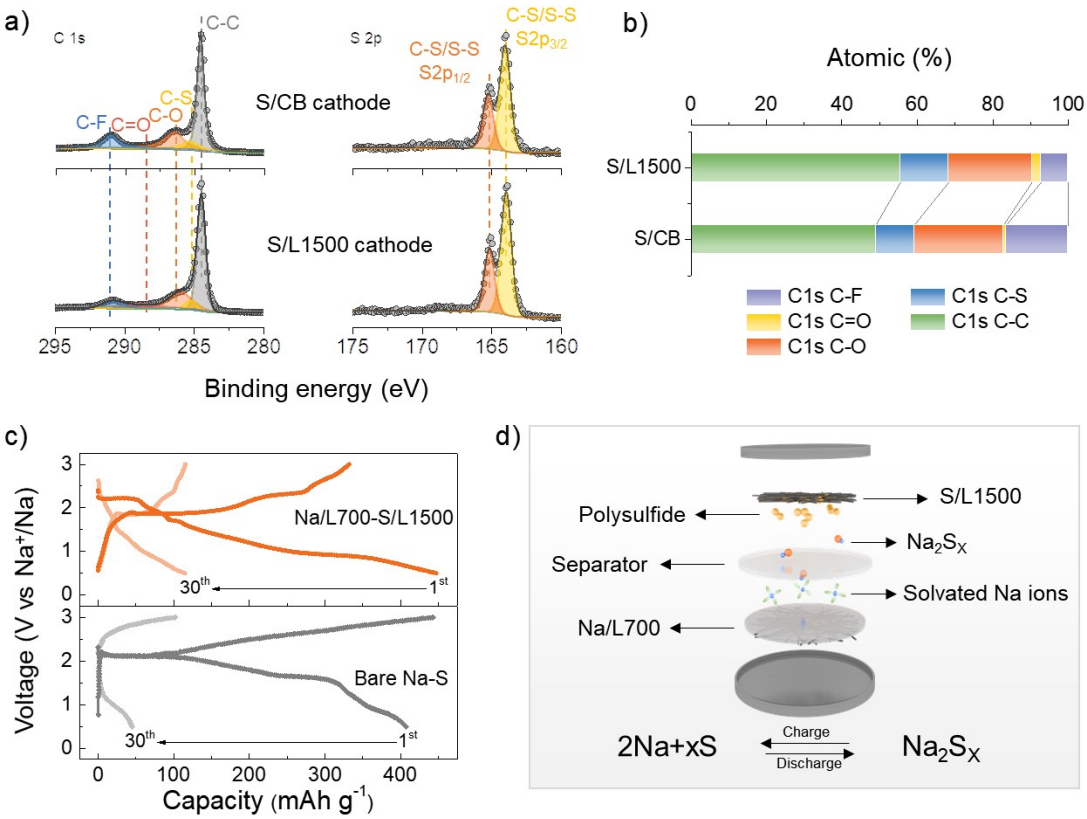

Figure S21. a) Fitted C 1s and S 2p core-level XPS spectra of the bare sulfur cathode (S/CB) and sulfur/L1500 cathode (S/L1500), and b) their corresponding atomic percentage; c) GCD curves of the full cells of Na/L700-S/L1500 and bare Na-S before and after cycling at 167.5 mA g^{-1}; d) Schematic illustration of sodium-sulfur batteries with the configuration of Na/L700 anode and sulfur/L1500 cathode (Na/L700-S/L1500);

The retention of the cycling performance still needs further efforts to be enhanced, which has been presented in the supporting information of this manuscript. The loss of capacity is mainly derived from the shuttle effect of the sulfur cathode. Our group is also focusing on the development of highly efficient carbon skeletons for sulfur cathodes, which is funded by the Faraday Institution's LiSTAr project (www.listar.ac.uk).

Table S1. Fitted terms including A, a_1, a_2, B_1 and B_2 from SAXS.

	A	a_1	a_2	B_1	B_2	C
L700	0.077	N/A	3.8	N/A	N/A	0.00499
L1100	0.46	3.3	N/A	7.8	0.72	N/A
L1500	0.28	2.8	N/A	11.9	1.48	N/A

Table S2. The atomic percentage of different elements (C, N, O) in L700, L1100 and L1500.

at %	C 1s						N 1s					O 1s			
	sp2	sp3	C-O	C=O	C-N	Total	N-6	N-5	N-Q	Ox-N	Total	O-I	O-II	O-III	Total
L700	18.99	32.84	18.10	9.19	9.06	88.18	0.52	0.75	0.58	0.40	2.25	1.05	6.09	2.43	9.57
L1100	35.81	19.70	22.49	12.21	2.90	93.11	0.34	0.58	0.11	0.55	1.73	0.59	3.09	1.48	5.16
L1500	42.12	15.58	24.64	14.75	-	97.09	-	-	-	-	N/A	0.22	1.45	1.24	2.91

at %: Atomic %

Ox-N: Oxidised N

Table S3. a) The calculated binding energy between sodium atoms (at different positions including centre and edges) and the graphene layers with(out) nitrogen doping, followed by b) the illustration of local charge densities between sodium atoms and graphene layers with(out) nitrogen doping.

a) Binding energy

Position	Plain	Pyridinic	Pyrrolic	Quaternary
Center	-0.77	-0.73	N/A	-1.90
Edge 1	-1.83	-1.81	-1.67	-2.08
Edge 2	-1.07	N/A	-0.99	-1.83
Edge 3	N/A	N/A	-0.74	-2.06

Unit: eV

b) Local charge densities

Position	Plain	Pyridinic	Pyrrolic	Quaternary
Centre	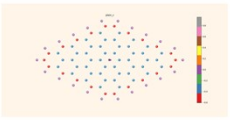	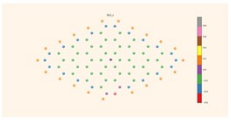	N/A	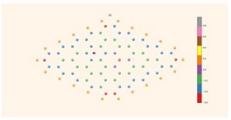
Edge 1	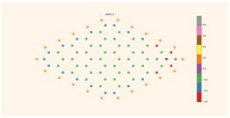	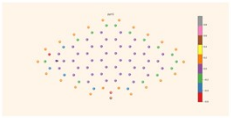	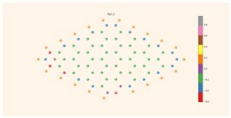	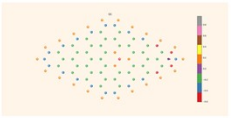
Edge 2	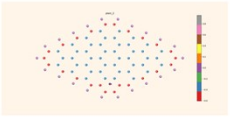	N/A	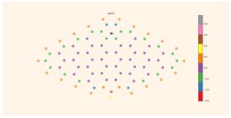	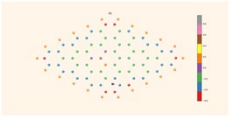
Edge 3	N/A	N/A	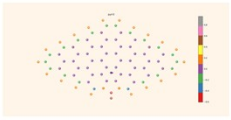	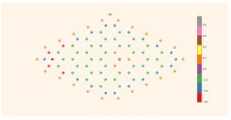

Table S4. Fitted elements of EIS of L700 at OCV, plated state and stripped state.

	R_s	R_{ct1}	R_{ct2}	R_{ct3}
OCV	15.3	74.4	N/A	N/A
Plated	4.6	10.8	15.2	N/A
Stripped	14.4	4.6	5.7	51.2

Unit: Ω

Table S5. Comparison of energy densities of sodium batteries

Sodium batteries (Anode-Cathode)	Energy density (Wh kg^{-1})	References
HCT-$Na_{0.9}[Cu_{0.22}Fe_{0.30}Mn_{0.48}]O_2$	207	*Adv. Energy Mater.* **2016**, 1600659 [21]
CCD-$NaNi_{1/3}Fe_{1/3}Mn_{1/3}O_2$	248	*J. Mater. Chem. A*, **2019**, 7, 27567 [22]
HC-$Na_{0.72}[Li_{0.24}Mn_{0.76}]O_2$	270	*Joule*, **2019**, 3, 503 [23]
Na/L700-PB	384	This work
Na/L700-S/L1500	567	This work

References

1. S. Hérou, M. Crespo Ribadeneyra, P. Schlee, H. Luo, L. Cristian Tanase, C. Roβberg and M. Titirici, *J. Energy Chem.*, 2021, **53**, 36-48.
2. S. Hérou, M. Crespo and M. Titirici, *CrystEngComm*, 2020, **22**, 1560-1567.
3. S. Herou, M. C. Ribadeneyra, R. Madhu, V. Araullo-Peters, A. Jensen, P. Schlee and M. Titirici, *Green Chem*, 2019, **21**, 550-559.
4. X. Wang, G. Pawar, Y. Li, X. Ren, M. Zhang, B. Lu, A. Banerjee, P. Liu, E. J. Dufek, J.-G. Zhang, J. Xiao, J. Liu, Y. S. Meng and B. Liaw, *Nat. Mater.*, 2020, **19**, 1339-1345.
5. Y. You, X. L. Wu, Y. X. Yin and Y. G. Guo, *Energy Environ. Sci.*, 2014, **7**, 1643-1647.
6. C. Zhou, J. Wang, X. Zhu, K. Chen, Y. Ouyang, Y. Wu, Y.-E. Miao and T. Liu, *Nano Res*, 2021, **14**, 1541-1550.
7. D. A. Stevens and J. R. Dahn, *J. Electrochem. Soc.*, 2000, **147**, 4428.
8. G. W. T. M. J. Frisch, H. B. Schlegel, G. E. Scuseria, M. A. Robb, J. R. Cheeseman, G. Scalmani, V. Barone, G. A. Petersson, H. Nakatsuji, X. Li, M. Caricato, A. Marenich, J. Bloino, B. G. Janesko, R. Gomperts, B. Mennucci, H. P. Hratchian, J. V. Ortiz, A. F. Izmaylov, J. L. Sonnenberg, D. Williams-Young, F. Ding, F. Lipparini, F. Egidi, J. Goings, B. Peng, A. Petrone, T. Henderson, D. Ranasinghe, V. G. Zakrzewski, J. Gao, N. Rega, G. Zheng, W. Liang, M. Hada, M. Ehara, K. Toyota, R. Fukuda, J. Hasegawa, M. Ishida, T. Nakajima, Y. Honda, O. Kitao, H. Nakai, T. Vreven, K. Throssell, J. A. Montgomery, Jr., J. E. Peralta, F. Ogliaro, M. Bearpark, J. J. Heyd, E. Brothers, K. N. Kudin, V. N. Staroverov, T. Keith, R. Kobayashi, J. Normand, K. Raghavachari, A. Rendell, J. C. Burant, S. S. Iyengar, J. Tomasi, M. Cossi, J. M. Millam, M. Klene, C. Adamo, R. Cammi, J. W. Ochterski, R. L. Martin, K. Morokuma, O. Farkas, J. B. Foresman, and D. J. Fox, *Gaussian 09 (Revision A.02), Gaussian, Inc., Wallingford CT*, 2016.
9. J. P. Perdew, K. Burke and M. Ernzerhof, *Phys. Rev. Lett.*, 1996, **77**, 3865-3868.
10. A. D. Becke, *J. Chem. Phys.*, 1993, **98**, 5648-5652.
11. E. D. Glendening, C. R. Landis and F. Weinhold, *J. Comput. Chem.*, 2013, **34**, 1429-1437.
12. A. C. Ferrari and D. M. Basko, *Nat. Nanotechnol.*, 2013, **8**, 235-246.
13. X. Ma, C. Yuan and X. Liu, *Materials (Basel)*, 2013, **7**, 75-84.
14. C. Bommier, T. W. Surta, M. Dolgos and X. Ji, *Nano Lett.*, 2015, **15**, 5888-5892.
15. P. Ge, S. Li, L. Xu, K. Zou, X. Gao, X. Cao, G. Zou, H. Hou and X. Ji, *Adv Energy Mater*, 2019, **9**, 1803035.
16. Z. Xu, F. Xie, J. Wang, H. Au, M. Tebyetekerwa, Z. Guo, S. Yang, Y. S. Hu and M. M. Titirici, *Adv. Funct. Mater.*, 2019, **29**, 1903895.
17. H. Au, H. Alptekin, A. C. S. Jensen, E. Olsson, C. A. O'Keefe, T. Smith, M. Crespo-Ribadeneyra, T. F. Headen, C. P. Grey, Q. Cai, A. J. Drew and M.-M. Titirici, *Energy Environ. Sci.*, 2020, **13**, 3469-3479.
18. W. Zhang, S. Zhang, L. Fan, L. Gao, X. Kong, S. Li, J. Li, X. Hong and Y. Lu, *Acs Energy Lett*, 2019, **4**, 644-650.
19. Y. Yang, D. M. Davies, Y. Yin, O. Borodin, J. Z. Lee, C. Fang, M. Olguin, Y. Zhang, E. S. Sablina, X. Wang, C. S. Rustomji and Y. S. Meng, *Joule*, 2019, **3**, 1986-2000.
20. J. B. Goodenough and Y. Kim, *Chem Mater*, 2010, **22**, 587-603.
21. Y. M. Li, Y. S. Hu, M. M. Titirici, L. Q. Chen and X. J. Huang, *Adv Energy Mater*, 2016, **6**, 1600659.
22. F. Xie, Z. Xu, A. C. S. Jensen, F. Ding, H. Au, J. Feng, H. Luo, M. Qiao, Z. Guo, Y. Lu, A. J. Drew, Y.-S.

Hu and M.-M. Titirici, *J. Mater. Chem. A*, 2019, **7**, 27567-27575.

23. X. Rong, E. Hu, Y. Lu, F. Meng, C. Zhao, X. Wang, Q. Zhang, X. Yu, L. Gu, Y.-S. Hu, H. Li, X. Huang, X.-Q. Yang, C. Delmas and L. Chen, *Joule*, 2019, **3**, 503-517.